J Geophys (1986) 60:1–18

Journal of Geophysics

Original investigations

Investigation of the velocity- and Q-structure of the lowermost mantle using *PcP/P* amplitude ratios from arrays at distances of 70°–84°

J. Schlittenhardt *

Institute of Meteorology and Geophysics, University of Frankfurt, Feldbergstrasse 47, D-6000 Frankfurt, Federal Republic of Germany

Abstract. Investigations of the core reflection *PcP* at distances in the neighbourhood of the core shadow zone are especially appropriate for the study of isolated regions of D″ because *PcP* for these distances has a large angle of incidence at the core-mantle boundary and is strongly influenced by the structure immediately above the core. A striking result of this investigation of *PcP* in the distance range 70°–84° is that *PcP* could be detected only in four cases (from a total of 16 earthquakes and 29 nuclear explosions) in the NORSAR- and GRF-array beams for *PcP*. This result is found although the *P*-wave-coda noise levels in the *PcP* beams are very low, mostly below the amplitude level of *PcP* predicted by standard earth models. In the cases where *PcP* could not be identified, the *PcP*/*P* amplitude ratio, which is estimated from the beams with the aid of a cross-correlation procedure, must be regarded as an upper limit for the actual *PcP*/*P* ratio. The interpretation of the *PcP*/*P* amplitude ratios with *one* radially symmetric, elastic model proved to be impossible. The generally small *PcP*/*P* ratios can be explained by lateral variations in seismic wave absorption within D″. Q_α values for short-period *P* waves in D″, between 800 (below Usbekistan) and 100 (below the northern Hudson Bay and Central Siberia), were found.

Several recent seismological investigations of the *P*- and *S*-wave velocity of the lowermost mantle have suggested velocity models with first-order discontinuities (with velocity increases of the order of 1.5%–3.0%) 150–300 km above the core-mantle boundary. Through the calculation of synthetic short-period seismograms and comparison with the array data compiled for the main part of this study, it is shown that such models are very unlikely to be a global feature if the *P* velocity jump is of the order of 2.5%–3.0%. Even models with reduced *P* velocity jumps of 1.3% produce clear onsets in short-period seismograms. They are not observed for *P* waves with ray paths bottoming beneath Central Siberia.

Key words: Lower mantle structure – D″ region – *PcP*/*P* amplitude ratios – Array data – Vespagrams – Matched filtering – Lower mantle discontinuities – Wave absorption

* *Present address:* Bundesanstalt für Geowissenschaften und Rohstoffe, Postfach 510153, D-3000 Hannover 51, Federal Republic of Germany

Introduction

The exact knowledge of the seismic wave velocities and Q-structure of the lowermost 100–200 km of the earth's mantle is of great importance for the understanding of the thermal and dynamical state of the earth's mantle as a whole. The simple conditions of chemical homogeneity and adiabaticity, which hold largely for the main part of the lower mantle and the outer core where the seismic wave velocities increase smoothly with depth, are possibly not valid within an approximately 200-km-thick zone directly above the core-mantle boundary [Bullen's (1950) zone D″] where the gradients of the wave velocities are possibly reduced or even negative. The physical significance of reduced or vanishing velocity gradients in this zone were first recognized by Bullen, who concluded from a hypothesis on the relation of compressibility and pressure (Bullen, 1949) that the density gradients within D″ are approximately three times greater than in a homogeneous medium. However, reduced or vanishing velocity gradients may also be explained by superadiabatic temperature gradients in chemical homogeneous material where thermal boundary layers develop. Within such boundary layers with increased temperature gradients [temperature differences of 1,000 K across D″ are discussed (Elsasser et al., 1979; Jeanloz and Richter, 1979)], the heat from the core is transferred by pure conduction and contributes to mantle-wide convection in the overlying mantle material (Jones, 1977; Peltier and Jarvis, 1982). Before being commonly accepted, however, these ideas about the state of the lowermost mantle should reflect, and find support in, the results of seismological work.

The methods which are applied to study the structure of the lowermost mantle with seismic body waves measure several different quantities of the waves interacting with the structure. Among these methods are measurements of the ray parameters of short- and long-period diffracted *P* and *S* waves (Gutenberg and Richter, 1936; Sacks, 1967; Cleary, 1969; Hales and Roberts, 1970; Bolt, 1970; Okal and Geller, 1979; Mula and Müller, 1980), determination of the decay constants of long-period diffracted *P* and *S* waves (Alexander and Phinney, 1966; Phinney and Alexander, 1966; Mondt, 1977; Doornbos and Mondt, 1979a, b; Mula, 1981; Doornbos, 1983), observation and interpretation of short-period precursors to *PKIKP* (Doornbos and

Husebye, 1972; King et al., 1974; Haddon and Cleary, 1974; Doornbos, 1978; Haddon, 1982) and of amplitude ratios *PcP/P* and *ScS/S* (Kanamori, 1967; Buchbinder, 1968; Ibrahim, 1971, 1973; Berzon et al., 1972; Buchbinder and Poupinet, 1973; Chowdhury and Frasier, 1973; Mitchell and Helmberger, 1973; Frasier and Chowdhury, 1974; Müller et al., 1977; Lay and Helmberger, 1983b). All these different investigations did not result in globally representative velocities at the base of the earth's mantle, and the question, of whether a zone with negative velocity gradient (velocity decrease with increasing depth) directly above the core-mantle boundary (CMB) exists or not, is still open. The only common result of these investigations is that the behaviour of body waves which sample the lowermost part of the mantle cannot be explained by simple extrapolation of the velocity gradients from the main part of the lower mantle (Cormier, 1985). Only recently, the partly spectacular results of seismic tomography of the earth's mantle (Dziewonski, 1984) established the D″ region as the region of the lower mantle with the greatest per cent lateral fluctuations of the seismic wave velocities. If such significant lateral variations exist, the question of the globally representative vertical velocity gradient loses some of its importance.

Matters are complicated even more by Lay and Helmberger's (1983a) proposal that a world-wide discontinuity in shear wave velocity exists about 280 km above the CMB. Their model, which has been derived by modelling the amplitudes and travel times of onsets betweeen mantle *S* and *ScS* in transverse-component seismograms at distances from 70° to 80°, predicts pronounced pulse-form changes of long-period *SH* waves in the epicentral distance range 95°–120°. Similar pulse-form changes are expected in *P*-wave seismograms, under the reasonable assumption of a similar increase in the *P* velocity. Schlittenhardt et al. (1985) compared nine long-period seismogram sections of *SH* and *P* waves from deep-focus earthquakes with synthetic seismograms for the PREM model (Dziewonski and Anderson, 1981) and the SLHO model of Lay and Helmberger and found practically no indication of the complications expected for the distance range 95°–120°.

The purpose of this paper is, therefore, two-fold. First, a new data set of short-period *PcP/P* amplitude ratios, derived from observations of the GRF array (Fed. Rep. Germany) and the NORSAR array (Norway) in the distance range 70°–84°, and the interpretation of these data with respect to the velocity gradients and *Q* structure at the base of the mantle, is presented. Secondly, short-period synthetic seismograms for *P* waves at distances from 70° to 100° that show pronounced differences between SLHO and PREM (which is of course expected) will be presented and compared to the short-period array data compiled for this study. It will be shown that, under the assumption of equal velocity jumps for the *P* and *S* velocity at the discontinuity of SLHO (we assumed 2.6% for both the *S*- and *P*-velocity jump), the existence of a world-wide discontinuity at the top of D″ can be disproved, in accordance with the findings from long-period data of Schlittenhardt et al. (1985). Values of the *P*-velocity increase of 1.3% and lower (keeping all other parameters in SLHO unchanged) can only be disproved by short-period data, as will be shown through comparison of synthetic seismograms with two selected observations.

Investigations of the core reflection *PcP* at distances in the neighbourhood of the core shadow zone are especially appropriate for the study of the velocity gradients at the base of the mantle. For these observation distances, *PcP* has a large angle of incidence at the CMB and is influenced strongly by the structure immediately above the core. *PcP* has been studied in the literature several times for epicentral distances up to 60°, mostly with the disappointing result of strong scatter in the observed *PcP/P* ratios. The reason for this scatter is probably the different *P* and *PcP* ray paths through the inhomogeneous (near-surface) regions of the earth with strongly different phase velocities (Frasier and Chowdhury, 1974). By utilizing the wavenumber characteristics of the NORSAR and GRF arrays and through the restriction to an observation range where the ray paths of *P* and *PcP* are nearly identical especially for their near-surface parts, effects which influence the amplitude behaviour of *P* and *PcP* in a *different manner* can be practically excluded. It is a reasonable assumption that the differences still remaining between observed *PcP/P* amplitude ratios and theoretical amplitude ratios for standart earth models like PREM must then be caused by structure in the lowermost mantle.

PcP/P amplitude ratios from array data in the distance range 70°–84°

For the distance range 70°–84°, the turning points of the mantle *P* wave lie in the depth range 1,900–2,500 km, a part of the lower mantle which is characterized by a smooth and uncomplicated distribution of material parameters. The difference in the take-off angle for *P* and *PcP* in that distance range decreases from 8.5° to 3°. It can be assumed therefore that inhomogeneities in the upper parts of the earth, where the ray paths of *P* and *PcP* are close, influence the amplitude behaviour of *P* and *PcP* in practically the same way and that the effects of such inhomogeneities cancel in the amplitude ratios. This qualitative argument can be quantified by ray-tracing calculations for spherical earth models: at an epicentral distance of 70°, the horizontal distance between a *P* and *PcP* ray at a depth of 670 km is 100 km (Spies, 1985). For a depth of 220 km (lithosphere), this distance decreases to approximately 20 km, which is already of the order of the wavelength of short-period *P* waves. Hence, at smaller depths the ray paths of *P* and *PcP* agree within one dominant wavelength. The essence of the amplitude-ratio method of this paper is therefore to model observed *PcP/P* amplitude ratios through variation of the elastic parameters and *Q* in the *lowermost* mantle. The amplitude modelling is done through the calculation of theoretical seismograms with the reflectivity method for vertically inhomogeneous media with arbitrary depth dependence of the specific dissipation *Q*.

As the difference travel time *PcP-P* is only approximately 7 s for an observation distance of 80°, events (earthquakes and nuclear explosions) with short and simple source pulses had to be selected. Besides this criterion, earthquakes selected for this study must have hypocentres deep enough that the surface reflection *pP* arrives after *PcP* and the focal mechanism must be orientated in such a way that *P* and *PcP* are radiated approximately with equal strength. Nine earthquakes with $m_b \geq 5.6$ recorded at GRF in the period 1976–1981 fulfilled these criteria (Table 1). For the time period of the full size of the NORSAR array (1971–1976), seven appropriate recordings from earthquakes with $m_b \geq 5.6$ could be selected (Table 1). Addition-

Table 1. List of earthquakes used for this study

No.	Region	Date	Origin time	Epicentre	Depth (km)	m_b	Δ (°)	PcP/P	R_{COR}	Fault plane solution from	Number of traces (sub-arrays)	Back-azimuth (°)	Azimuth (°)
Earthquakes observed at GRF													
1	S. of Okhotsk	10.07.76	11:37:14.0	47.31 N 145.75 E	402	5.8	75.7	0.10	1.09	++	3	30	331
2	Kuriles Is.	14.08.78	18:46:23.4	49.83 N 156.32 E	80	5.7	76.4	0.05	–	+	6	22	338
3	Fox Is.	01.09.79	05:27:17.6	53.98 N 165.20 W	69	5.8	76.7	0.07	1.36	+	5	2	358
4	Rat Is.	18.10.79	03:35:26.9	51.86 N 177.13 E	62	6.0	78.1	0.17	1.17	+	10	9	351
5	Kuriles Is.	04.10.78	03:54:15.2	46.25 N 151.80 E	86	5.6	78.5	0.09	0.88	+	5	27	335
6	Kuriles Is.	22.09.76	00:16:06.6	44.78 N 149.21 E	58	6.1	79.0	0.10	–	+	2	29	334
7	Kuriles Is.	19.03.77	10:56:22.0	44.20 N 148.20 E	70	6.0	79.3	0.07	0.99	+	3	30	333
8	Kuriles Is.	03.09.81	05:35:44.8	43.62 N 147.03 E	45	6.6	79.4	0.07	0.89	+++	13	31	333
9	Honshu, Jap.	24.09.80	17:54:24.1	35.45 N 139.96 E	73	6.0	83.9	0.06	0.95	++	13	40	329
Earthquakes observed at NORSAR													
10	Sea of Jap.	10.06.71	19:59:53.3	41.10 N 138.52 E	233	5.6	69.9	0.09	1.44	++	22	40	336
11	Ryukyu Is.	26.10.72	17:05:05.6	27.48 N 128.57 E	63	6.0	78.6	0.05	0.98	+	22	53	334
12	N. of Taiwan	11.09.73	23:18:50.4	25.65 N 124.58 E	137	5.7	78.6	0.09	–	+	12	57	333
13	S. of Honshu	04.03.71	00:28:38.3	30.41 N 138.44 E	449	5.6	79.6	0.07	1.00	+	21	44	337
14	Nicobar Is.	05.08.76	13:37:14.7	7.00 N 94.31 E	87	5.7	80.8	0.13	0.63	+	20	92	330
15	Nicobar Is.	17.07.71	05:32:43.4	6.98 N 94.65 E	144	5.6	80.9	0.12	0.83	+	22	92	330
16	Bonin Is.	13.11.72	08:11:49.3	27.93 N 140.14 E	374	5.6	82.5	0.05	1.00	+	22	44	338

\+ , Fault-plane solution based on polarity readings of the ISC;
++ , Fault-plane solution based on own polarity readings of WWSSN-LP seismograms;
+++ , Fault-plane solution by Needham (based on polarity readings), as published in the 'Monthly Listings, PDE' of the USGS

For explanation of the other parameters see text. Sources: ISC and USGS

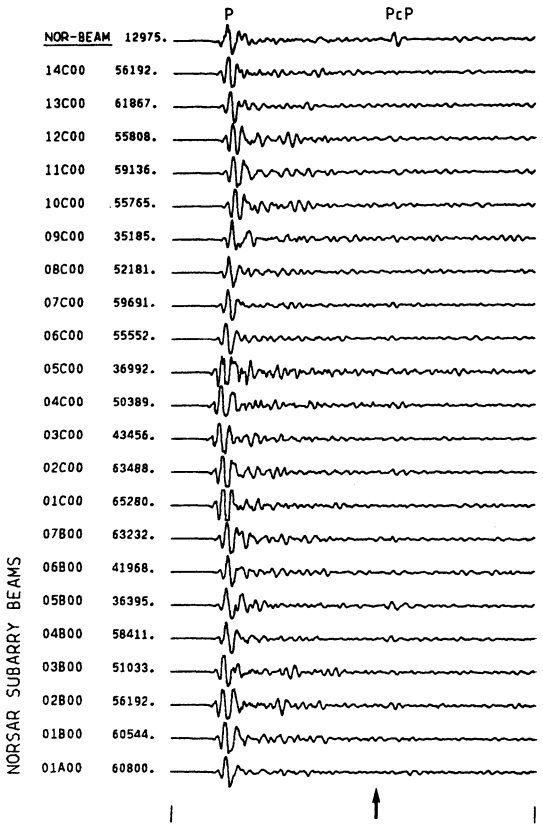

Fig. 1. NORSAR subarray beams and array beam (*uppermost trace*) for *PcP* for earthquake No. 10 from Table 1. To the left of the seismograms, subarray codes and the maximum peak-to-peak amplitudes, respectively, are given. *The arrow* indicates the Herrin arrival time for *PcP*. The duration of the time window is 45 s

ally, from this period, recordings of 28 nuclear explosions at the Nevada Test Site, USA and of one explosion in Colorado, USA (No. 6 in Table 2) could be found. The geographical position of the epicentres of these events is shown in Fig. 11.

Estimation of the PcP/P amplitude ratio from correlograms of P and PcP array beams

Following e.g. Harjes and Henger (1973) or Kelly (1967), the array response function for monochromatic plane waves of the GRF and NORSAR array has been calculated (Schlittenhardt, 1984) to determine how much *P*-wave energy can be suppressed in the *PcP* beam when the arrays are tuned to the slowness of *PcP*. It turned out that for all earthquakes and nuclear explosions recorded at the NORSAR array (except No. 16 in Table 1) the wavenumber difference of *P* and *PcP* (assuming a dominant signal frequency of 1 Hz) is greater or equal to the minimum wavenumber difference $\vec{k}_{\min}$ which is necessary to reach the rejection band of the array response function. This means that the amplitude reduction of *P* waves in the NORSAR *PcP* beams is -13 dB. For the GRF array, the situation is not as favourable because most of the events analysed are from times before the full configuration of the array had been completed.

The theoretical expectations concerning the *P*-wave amplitude reduction in the *PcP* beams could be verified in the course or our data analysis. This is illustrated in Fig. 1 where the NORSAR-subarray beams and the *PcP* array beam are shown for event No. 10 from Table 1. The reduction of the *P*-wave and *P*-wave-coda amplitudes in the *PcP* beam by a factor of approximately 0.22 (-13 dB) leads to a significant noise reduction at the arrival time of *PcP* and makes possible the emergence of the *PcP* signal. This is especially obvious when one compares the noise levels of the subarray beams and the array beam.

The data example has demonstrated the necessity and usefulness of simple beam-forming to detect the rather weak *PcP* signal in the coda of *P*. Therefore, for the investigation of the 44 events selected for this study, the *P* and *PcP* beams were calulated and plotted with equal amplitude scale to determine the *PcP*/*P* amplitude ratio by measuring the peak-to-peak amplitude. In the course of this analysis it turned out that *PcP* is characterized by very small amplitudes and that *PcP* could be detected reliably in only four cases, although the noise level at the arrival time of *PcP* is well below the expected amplitude level of *PcP*, e.g. for the PREM model. In all other cases one has to solve the problem of measuring the amplitude of a signal which is hidden in a time series with superimposed noise. In our special case here however, the problem reduces to the measurement of the amplitude of a signal with known *shape* which is hidden in noise: from the evidence of observations of short-period *PcP* waves (at smaller epicentral distances) one generally expects a no more complicated wave-form for the core reflection than for the direct *P* wave (Kanamori, 1967). The best existing data, namely the LASA-array beams for *P* and *PcP* (Chowdhury and Frasier, 1973; Frasier and Chowdhury, 1974; Engdahl and Johnson, 1974), show a reproduction of the pulse-form of *P* for *PcP*. To solve this kind of problem in digital signal processing (e.g. Lüke, 1979; Kanasewich, 1975), the correlation-filter or matched-filter technique is successfully applied. This method will be used throughout this study to estimate the *PcP*/*P* amplitude ratio.

Matched filtering of PcP beams. The matched filtering of *PcP* beams is performed through the calculation of the cross-correlation function $\Phi_{sx}(t)$ (filter output) of the time series $x(t)$ (here the *PcP* beam) and the signal $s(t)$ (here the *P* pulse with duration T defined in the *P* beam):

$$\Phi_{sx}(t)=\int_{-\infty}^{\infty} s(\tau)\,x(\tau+t)\,d\tau. \tag{1}$$

Assuming for the *PcP* beam $x(t)$:

$$x(t)=a\,s(t-t_0)+n(t), \tag{2}$$

where $a\,s(t-t_0)$ is the *PcP* signal with arrival time t_0 and $n(t)$ is the noise. Inserting Eq. (2) into Eq. (1) yields

$$\begin{aligned}\Phi_{sx}(t)&=\int_{-\infty}^{\infty}[a s(\tau)\,s(\tau-t_0+t)+s(\tau)\,n(\tau+t)]\,d\tau\\&=a\Phi_{ss}(t-t_0)+\Phi_{sn}(t).\end{aligned} \tag{3}$$

$\Phi_{ss}(t-t_0)$ is the auto-correlation function Φ_{ss} shifted by the time t_0. The auto-correlation function $\Phi_{ss}(t-t_0)$ has its maximum at time $t=t_0$, the arrival time of *PcP*. Now we normalize Eq. (3) to the maximum of the auto-correlation function

$$\Phi_{ss}(0)=\int_0^T s^2(\tau)\,d\tau:$$

$$\Phi_{sx}^{\mathrm{nor}}=a\left[\frac{\Phi_{ss}(t-t_0)}{\Phi_{ss}(0)}\right]+\frac{\Phi_{sn}(t)}{\Phi_{ss}(0)}. \tag{4}$$

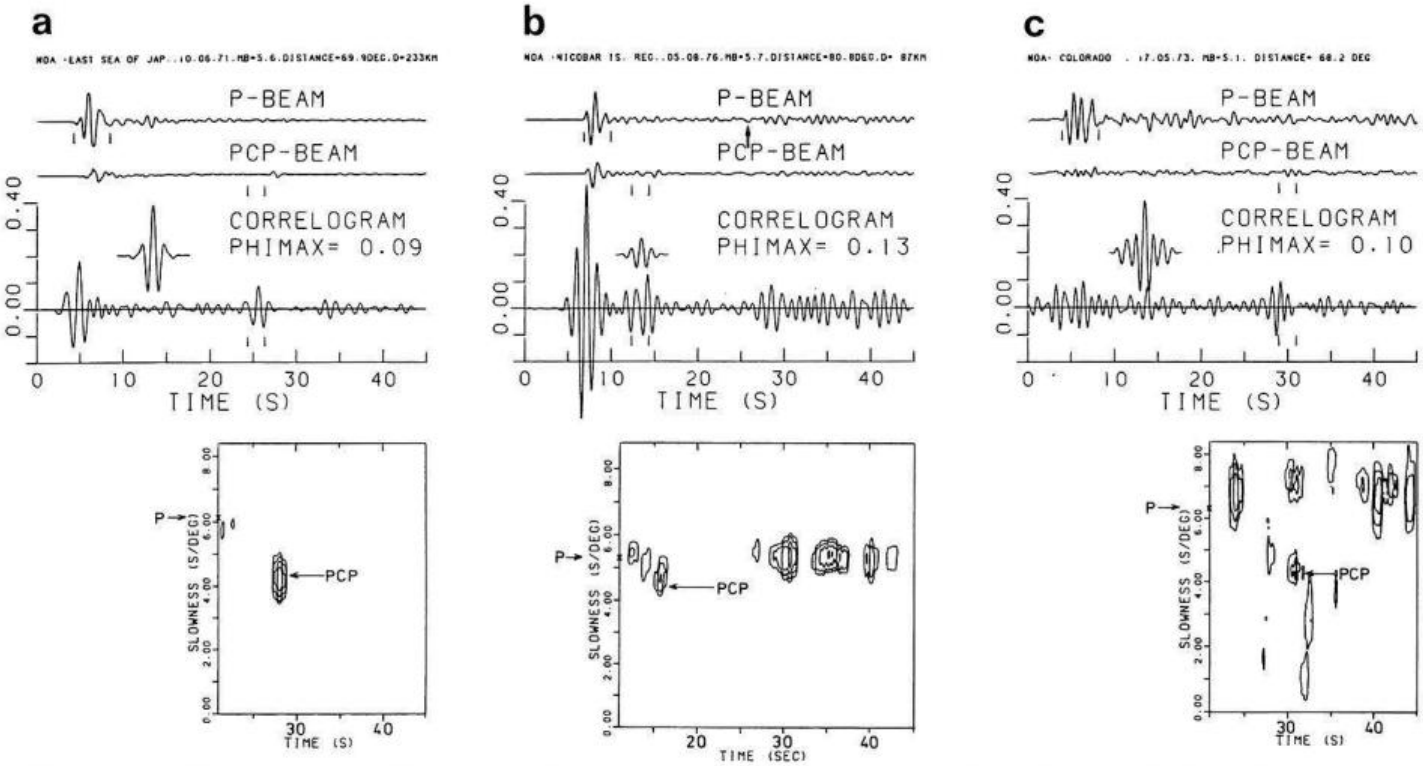

Fig. 2. **a** *P*, *PcP* beam, correlogram (*upper part*) and vespagram (*lower part*) for earthquake No. 10 from Table 1. The contour interval for the isolines in the vespagram is −3 dB. *The arrows* mark the slowness for *P* and *PcP*, respectively, after the Herrin tables. **b** The same as in Fig. 2a for earthquake No. 14 from Table 1. *The arrow* in the *P* beam marks the theoretical arrival time of the surface reflection *pP*. **c** The same as in Fig. 2a for the nuclear explosion in Colorado (No. 6 in Table 2)

The first term in the sum in Eq. (4), at time $t=t_0$, yields the desired amplitude ratio a. The second term in Eq. (4) corresponds to the normalized cross-correlation function of $s(t)$ and the noise $n(t)$. Taking into account that the noise mostly represents *P*-coda waves which are suppressed in the *PcP* beam, it can be assumed that $\Phi_{sn}(t)\approx 0$. Then Φ_{sx}^{nor} in Eq. (4) yields, at time $t=t_0$, the desired amplitude ratio a. This procedure for matched filtering of *P* and *PcP* array beams is illustrated in Fig. 2a for the Sea of Japan earthquake (No. 10 in Table 1). The upper part of this figure shows the *P* and *PcP* beam (plotted with equal amplitude scale) and the corresponding correlogram Φ_{sx}^{nor} according to Eq. (4). In the left part of the correlogram, the auto-correlation $\Phi_{ss}(t)$ for the signal $s(t)$ defined in the *P* beam is plotted for purposes of comparison. In the lower part of this figure, a vespagram for the last 25 s of the data window is shown. The *P* signal $s(t)$ is defined in the *P* beam by a pair of vertical bars. The pairs of vertical bars in the *PcP* beam and correlogram correspond to the minimum- and maximum-difference travel-time *PcP-P*, derived for two models with extremely positive and negative velocity gradients at the base of the mantle (P190 and N190 in Fig. 8). Additionally, for all events studied, these individually calculated minimum and maximum theoretical travel times were decreased and increased, respectively, by 1 s to take into account the finite width of the auto-correlation function for a signal with a dominant frequency of 1 Hz. The wanted *PcP/P* amplitude ratio a from Eq. (4) (denoted PHIMAX in Fig. 2a) is determined as the maximum of the correlogram Φ_{sx}^{nor} in the *PcP* arrival-time window. Our theoretical minimum and maximum travel times thus define a *PcP* arrival-time window whose limits are given by the maximum possible range of variability for the *PcP-P* difference travel time for currently discussed gradient models. In Fig. 2a, the form of the auto-correlation function is in good agreement with the form of the correlogram in the arrival-time window for *PcP*, as expected of course. The peak of the correlation signal corresponds to the arrival time of *PcP* and lies within the predicted arrival-time window, as does the onset of the *PcP* signal in the *PcP* beam. The main peak and trough of the *PcP* signal (compare with the form of the *P* signal in the *P* beam) can be recognized shortly after the maximum arrival time for *PcP*. In the vespagram in the lower part of Fig. 2a, *PcP* causes a sharp maximum in the slowness-versus-time plane; this confirms again that it is possible to identify the rather weak *PcP* signals in the range 70°–84°.

Earthquake data

Despite the rather small difference in take-off angles of *P* and *PcP*, a bias of the *PcP/P* amplitude ratios because of unequal radiation at the source is possible. Therefore, we tried to construct fault-plane solutions for all investigated earthquakes. For most of the earthquakes the first-motion data as published in the ISC bulletin were used (Table 1). There are inconsistencies in the polarity distributions derived from these data, but for all earthquakes investigated it is possible to make a decision as to whether the generally very small *PcP/P* amplitude ratios determined in this paper are caused by nodal radiation of *PcP* or not. The fault-plane solutions and polarity distributions for all earthquakes investigated are shown in Fig. 3. For those earthquakes for which a reliable determination of the fault-

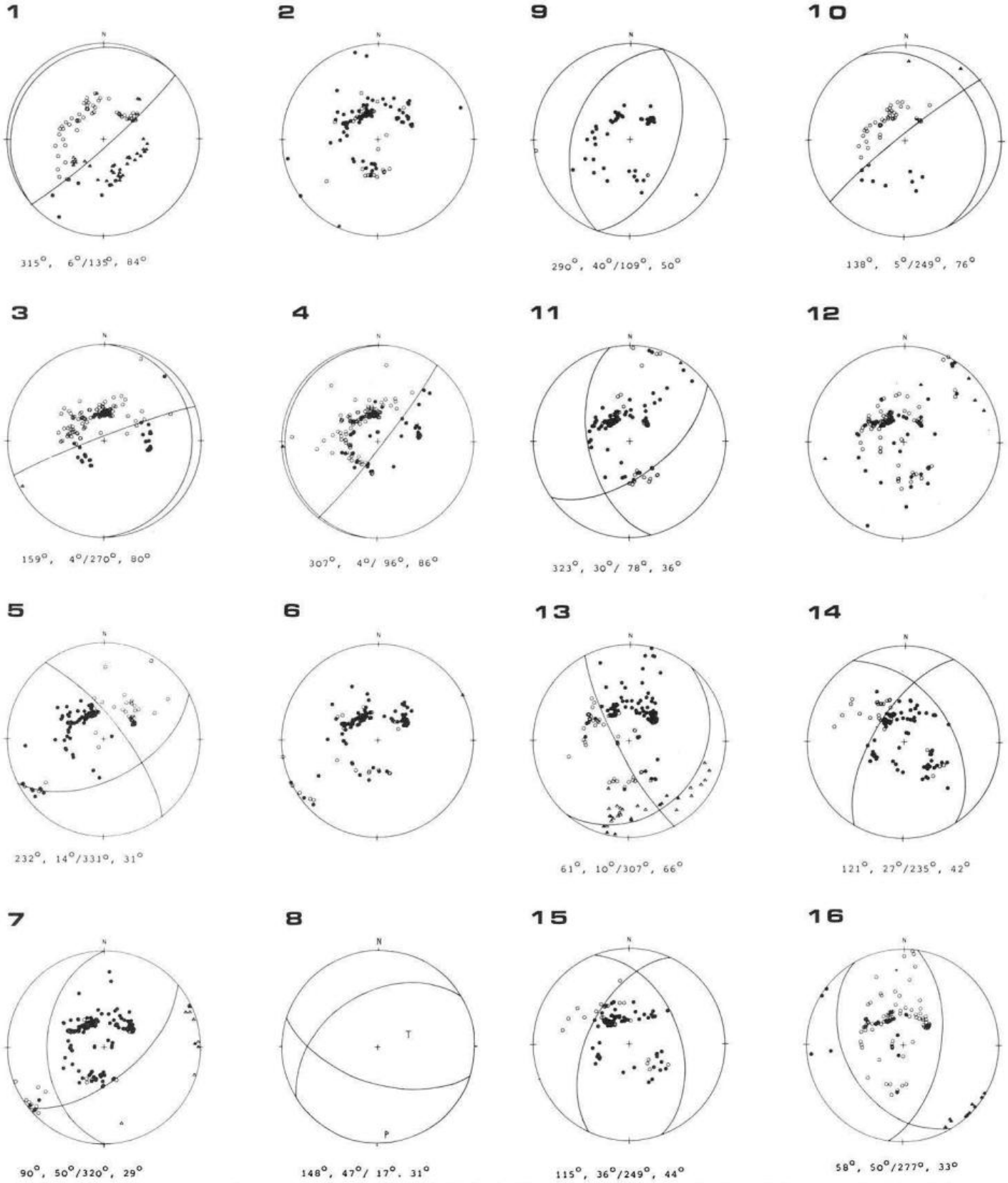

Fig. 3. Fault-plane solutions for the earthquakes listed in Table 1, shown as equal-area projections of the lower focal hemisphere. *Open* (*solid*) *symbols* indicate dilatation (compression). No attempt was made to draw the nodal planes for events 2 and 6. For event 8, a graphical representation of the fault-plane solution by Needham from the 'Monthly Listings, PDE' of the USGS is shown. The numbers below the fault-plane solutions indicate the trend and plunge of the poles of the P nodal planes

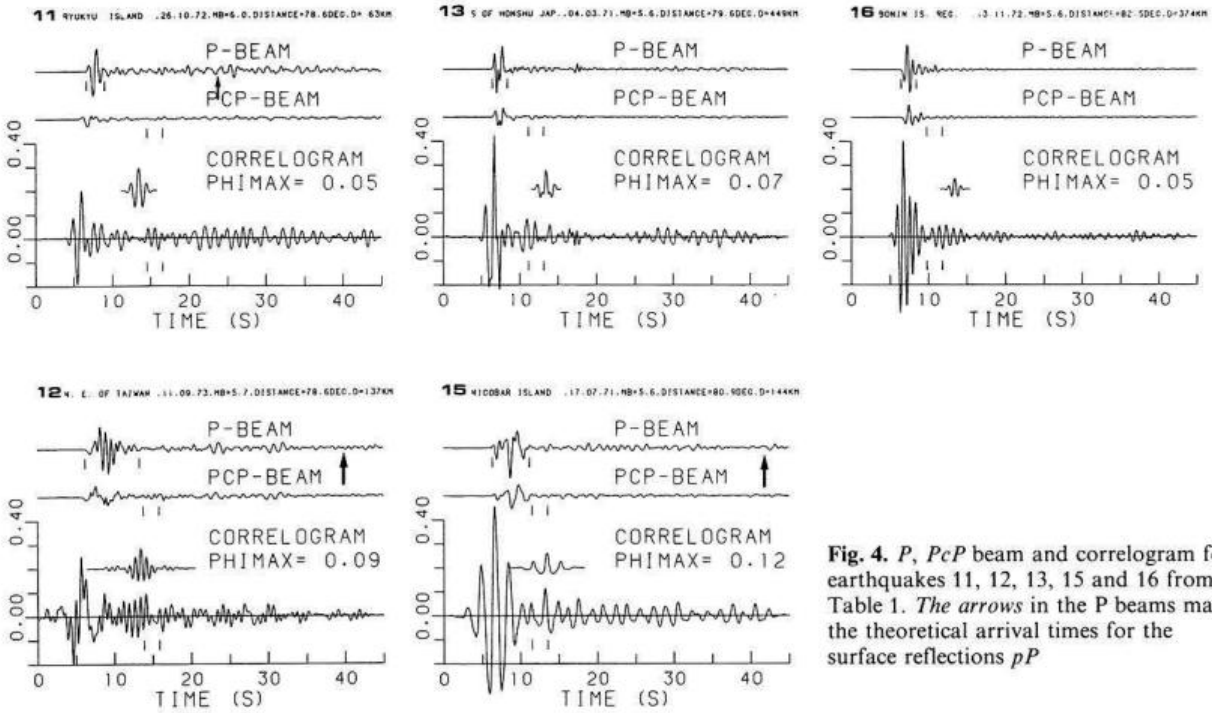

Fig. 4. *P*, *PcP* beam and correlogram for earthquakes 11, 12, 13, 15 and 16 from Table 1. *The arrows* in the P beams mark the theoretical arrival times for the surface reflections *pP*

plane solution was possible, a correction factor $R_{cor} = A_P / A_{PcP}$ for isotropic source radiation was calculated (Table 1), where A_P and A_{PcP} are the relative far-field radiations for *P* and *PcP* for the respective double-couple point source (Aki and Richards, 1980).

Recordings from NORSAR. The recordings from earthquakes recorded at the NORSAR array (Nos. 10–16 in Table 1) were processed as was illustrated for the Sea of Japan earthquake; they are presented in Figs. 2b and 4. For earthquake No. 14, the second one with identifiable *PcP* signal, a velocity-spectral analysis was made in addition to the matched-filtering: as in the case of the Sea of Japan earthquake the main minimum and maximum of the *PcP* signal can be identified in the *PcP* beam shortly after the maximum *PcP* arrival time, and the forms of the auto-correlation function and the correlogram in the corresponding arrival-time window are in good agreement (Fig. 2b). In the slowness-versus-time plane, *PcP* causes an isolated peak (lower part of Fig. 2b). For all other earthquakes in Fig. 4, despite the significant reduction of *P*-coda noise in the *PcP* beam, *PcP* could not be detected reliably, although at least in some cases (e.g. No. 16 in Fig. 4) the forms of the auto-correlation function of the *P* signal and the correlogram in the corresponding arrival-time window are relatively similar.

Recordings from GRF. The recordings from the nine earthquakes recorded at the GRF array (Nos. 1–9 in Table 1) are presented in Fig. 5. Because wavenumber difference increases with increasing frequency (at a given slowness difference for *P* and *PcP*) and because of the corresponding improvement in wavenumber filter capability of an array, it is appropriate to use short-period seismograms of the originally broadband GRF data. In this paper we work with short-period simulations of the broadband GRF data, according to the transfer function of a WWSSN-SP station (Seidl, 1980). The treatment of the GRF data in Fig. 5 is analogous to that for the NORSAR data except that the plot of the auto-correlation of the *P* signal has been omitted. The reason for this is that the amplitude reduction of *P*-wave energy in the *PcP* beam is not very strong for most of the earthquakes, because they are form the time period before the full-size operation of the array. For those events with only a small reduction of *P*-wave energy in the *PcP* beam (e.g. No. 1 in Fig. 5), one obtains a function in the correlograms at the *P* arrival time which is very similar to the actual auto-correlation function and which can be compared with the form of the correlogram in the predicted arrival-time window for *PcP*. *PcP* can be detected in none of the recordings in Fig. 5, neither in the beam-trace at the predicted arrival-time window nor in the correlogram through comparison with the quasi auto-correlation function. PHIMAX in Fig. 5 is again the maximum of the correlogram [Eq. (4)] in the time window marked by a pair of vertical bars.

Explosion data

The source parameters of the 29 nuclear explosions recorded at the NORSAR array are given in Table 2. Besides one explosion in Colorado (No. 6) all other explosions were detonated at the Nevada Test Site (NTS). The majority of the recordings are presented in Fig. 6, with the plot of the auto-correlation function inserted in the correlogram. The remaining recordings from NTS explosions (presented in Schlittenhardt, 1984) have essentially the same information content (with regard to this study) and are not reproduced here. The mean distance from the NTS explosions to NORSAR is 73.2°. The record of the Colorado explosion is presented in Fig. 2c. This event at a distance of 68.2° from NORSAR is, besides the Sea of Japan and Nicobar Island earthquakes (Nos. 10 and 14 in Table 1), the third

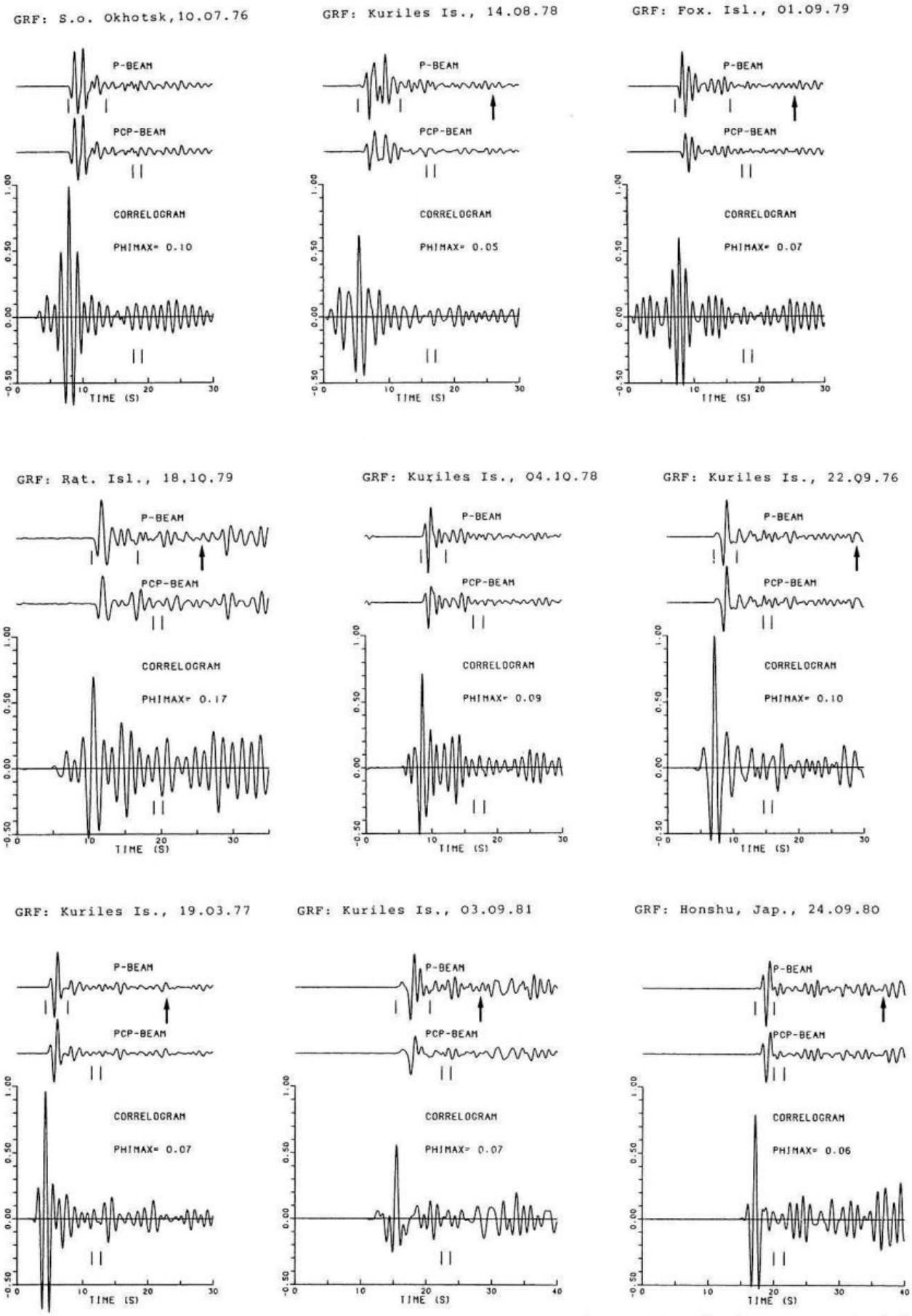

Fig. 5. *P*, *PcP* beam and correlogram for earthquakes 1–9 (from left to right) from Table 1. All seismograms are simulations of the original GRF broadband data according to the transfer function of a short-period WWSSN seismometer. The *arrows* in the *P* beams mark the theoretical arrival times of the surface reflection *pP*

Table 2. Source parameters and other parameters for the 28 explosions at the Nevada Test Site (NTS) and the nuclear explosion in Colorado (No. 6), recorded at NORSAR. The mean distance to the NTS events is 73.2°. The explosion in Colorado was at a distance of 68.2° from NORSAR. Source: ISC

No.	Date	Origin time	Epicentre	m_b	*PcP*/*P*	Number of subarrays
01	08.07.71	14:00:00.1	37.11N 116.05W	5.5	0.05	21
02	18.08.71	13:59:59.3	36.99N 116.06W	5.3	0.02	19
03	21.09.72	15:30:00.2	37.08N 116.04W	5.6	0.03	20
04	08.03.73	16:10:00.2	37.10N 116.03W	5.3	0.02	22
05	26.04.73	17:15:00.2	37.12N 116.06W	5.6	0.06	22
06	17.05.73	16:00:00	39.79N 108.37W	5.1	0.10	22
07	05.06.73	17:00:00.2	37.18N 116.21W	5.0	0.06	22
08	06.06.73	13:00:00.1	37.25N 116.35W	6.1	0.03	19
09	27.02.74	17:00:00.1	37.10N 116.05W	5.6	0.05	21
10	10.07.74	16:00:00.1	37.07N 116.03W	5.7	0.03	19
11	30.08.74	15:00:00.2	37.15N 116.08W	5.6	0.02	22
12	26.09.74	15:05:00.2	37.13N 116.07W	5.5	0.05	21
13	28.02.75	15:15:00.1	37.11N 116.06W	5.6	0.03	22
14	07.03.75	15:00:00.2	37.13N 116.08W	5.4	0.05	22
15	14.05.75	14:00:00.4	37.22N 116.47W	5.9	0.07	20
16	03.06.75	14:20:00.2	37.33N 116.52W	5.8	0.10	20
17	03.06.75	14:40:00.1	37.09N 116.03W	5.6	0.03	20
18	19.06.75	13:00:00.1	37.35N 116.32W	5.9	0.03	19
19	28.10.75	14:30:00.2	37.28N 116.41W	6.2	0.04	21
20	20.11.75	15:00:00.1	37.22N 116.37W	5.9	0.04	20
21	20.12.75	20:00:00.2	37.12N 116.06W	5.6	0.04	21
22	03.01.76	19:15:00.2	37.30N 116.33W	6.2	0.04	21
23	12.02.76	14:45:00.2	37.27N 116.49W	6.1	0.06	21
24	14.02.76	11:30:00.2	37.24N 116.42W	5.8	0.03	21
25	09.03.76	14:00:00.1	37.31N 116.36W	5.8	0.05	21
26	14.03.76	12:30:00.2	37.31N 116.47W	6.2	0.07	21
27	17.03.76	14:15:00.1	37.26N 116.31W	6.0	0.05	21
28	17.03.76	14:45:00.1	37.11N 116.05W	5.8	0.01	21
29	26.08.76	14:30:00.2	37.13N 116.08W	5.3	0.06	21

event with an identifiable *PcP* signal. *PcP* can be detected in the *PcP* beam as well as in the correlogram and in the vespagram within the predicted arrival-time window. The *P*-wave and *P*-wave-coda amplitude reduction in the *PcP* beams of Fig. 6 is so strong that the *PcP* beams nearly become straight lines. At the same time, in none of the beam traces can a clear indication for the emergence of a *PcP* signal in the predicted arrival-time window be found. However, at least in some of the correlograms in Fig. 6 (e.g. for the events 1, 5, 9 and 13) the form of the correlogram in the *PcP* arrival-time window is relatively similar to the form of the corresponding auto-correlation function of the *P* signal. This suggests that *PcP* begins to stand out from the noise at PHIMAX values between 0.03 and 0.06 (Fig. 6). The mean value of all PHIMAX values for the explosions at the Nevada Test Site is 0.045, with a standard deviation of 0.018. This mean value is close to the PHIMAX values of those events for which the emergence of *PcP* is suggested through comparison of the correlation functions and is therefore interpreted to represent a close estimate for the actual *PcP*/*P* amplitude ratio for the observation geometry NTS-NORSAR.

Amplitude ratios PcP/P

To summarize, it can be stated that for the 16 investigated earthquakes with simple and short source pulses, *PcP* can be detected reliably in only two cases. Taking into account that practically no indication for the appearance of a *PcP* signal can be detected for the other events studied, neither in the *PcP* beams nor in the correlograms of Figs. 2a and b, 4 and 5, the uniformly determined PHIMAX values must be regarded as an upper limit for the actual, very small *PcP*/*P* amplitude ratio. In the presentation of the results in Fig. 7 these values are plotted as heavy dots on vertical bars to indicate that the true *PcP*/*P* amplitude ratios lies somewhere between the abscissa and the heavy dot. The values for the two events with identifiable *PcP* signal are plotted as encircled dots ('Jap' and 'Nicobar Is.'), for the NTS explosions the mean value and standard deviation of all PHIMAX values from the NTS explosions in Table 2 are plotted ('NTS'), and the amplitude ratio for the nuclear explosion in Colorado is given ('Co'). To comment on the reliability of this result of generally very small *PcP*/*P* amplitude ratios, it can be said that a systematic source or receiver effect, that leads to an underestimation of the *PcP*/*P* ratio for *all* events, can be practically excluded because of the different source regions and ray paths of the events studied. That nodal radiation of *PcP* is the cause of the non-observability of *PcP* can be excluded because of the fault-plane solutions for the earthquakes studied: the correction factor for isotropic radiation (R_{cor} in Table 1) is close to one or smaller for most of the earthquakes studied.

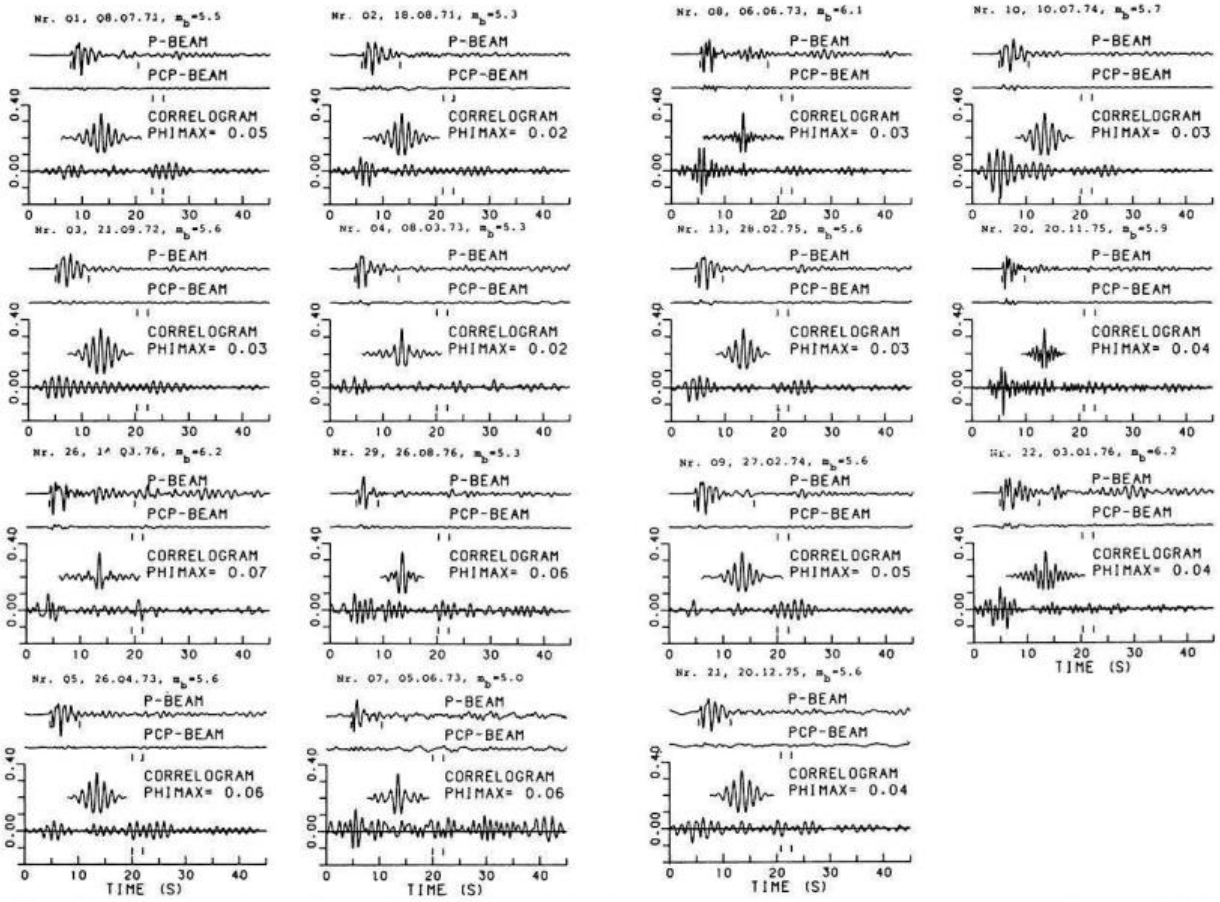

Fig. 6. *P*, *PcP* beam and correlogram for nuclear explosions from the Nevada Test Site (numbering according to Table 2)

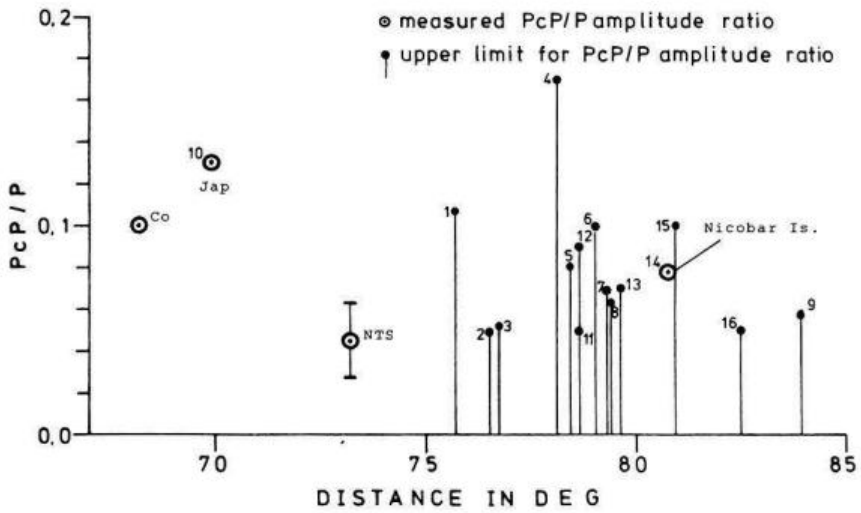

Fig. 7. *PcP*/*P* amplitude ratios for events with identifiable *PcP* signal (⊙) and upper limit for the *PcP*/*P* amplitude ratio for events without identifiable *PcP* signal (📍) for the earthquakes from Table 1 (with corresponding numbering) and for the nuclear explosions from Table 2. The value marked 'NTS' corresponds to the mean value (with *bars* indicating standard deviations) of all PHIMAX values from the nuclear explosions from the Nevada Test Site. 'Co' corresponds to the value for the nuclear explosion in Colorado (No. 6 in Table 2). All earthquake data have been corrected for isotropic source radiation

Amplitude behaviour of *PcP* for changes in the elastic parameters on both sides of the CMB and for increased absorption in D''

The models

The starting point for the theoretical investigation of the amplitude behaviour of *P* and *PcP* was the isotropic (1 Hz) PREM model of Dziewonski and Anderson (1981). Figure 8 shows the *P*- and *S*-wave velocity of this model for the lowermost 300 km of the mantle. In this model, the lowermost mantle is characterized by a second-order discontinuity 150 km above the core-mantle boundary. Starting at a depth of 2,700 km, three further models (P190, M190, N190) marked with an open square, circle and triangle are plotted. The dashed line in Fig. 8 defines a model with an extreme, positive velocity gradient in a 190-km-thick zone. Additionally, two models (P75 and N75) with

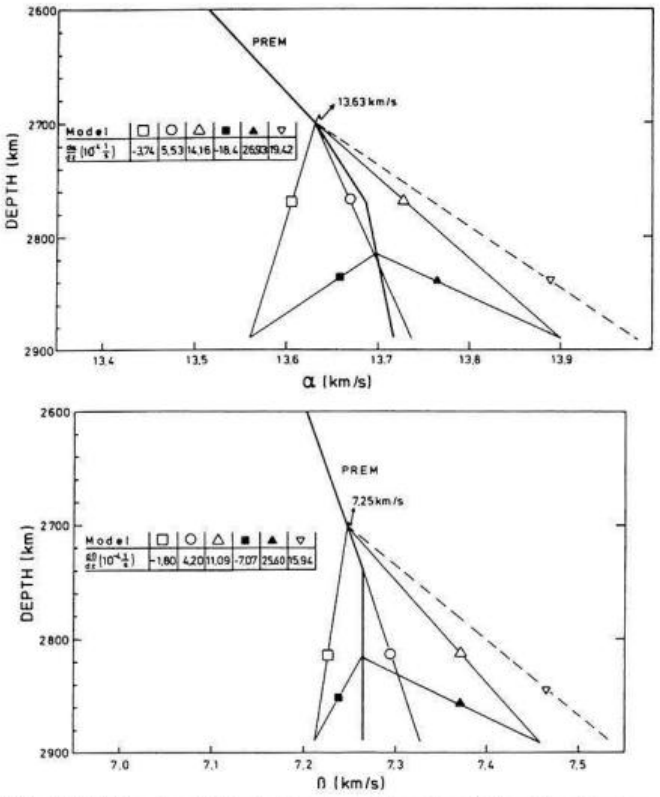

Fig. 8. P (*above*) and S velocity-depth function (*below*) for the lowermost mantle of the earth with corresponding P- and S-velocity gradients $\frac{d\alpha}{dz}$ and $\frac{d\beta}{dz}$. The *heavy line* correponds to the PREM model of Dziewonski and Anderson (1981). The other models are named in the text as follows: □: N190, ○: M190, △: P190, ■: N75, ▲: P75, ▽: extreme, positive velocity gradient

increased positive and negative velocity gradients in thin zones of 75 km thickness are marked with a full square and triangle. The three models which vary in 190-km-thick zones above the CMB correspond to the mean value (M190) and standard deviations (P190 and N190) of ray-parameter measurements of long-period P_{diff} and S_{diff} for a great number of earthquakes studied by Mula and Müller (1980). They can be regarded as limiting the model space for linear gradient models in zones of 190 km thickness. All models presented in Fig. 8 have Poisson's ratios near 0.3 at the CMB.

For these models, synthetic seismogram sections for P and PcP were calculated with an extended reflectivity method (Müller, 1985). In these calculations the elastic model structure is the same as for PREM at depths less than 2,700 km and the Q structure is identical with that of PREM for the whole mantle and the outer core. A constant-Q law which preserves causality was assumed in the calculations. Theoretical PcP/P amplitude ratios were determined from the record sections by measuring the peak-to peak amplitudes of P and PcP. The resulting PcP/P amplitude ratios for the models M190, P190 and N190 are plotted in Fig. 9 as the uppermost dotted band of three amplitude-ratio distance curves. The denotation $Q_\alpha = 826$ (PREM value for D″) in Fig. 10 indicates the Q_α value in a zone of 190 km thickness directly above the CMB. The theoretical PcP/P amplitude-ratio distance curves for models P75 and N75 cannot be distinguished from those for models P190 and N190 if the Q structure of PREM is assumed for all models and if one calculates for a purely elastic structure, respectively. Corresponding theoretical amplitude-ratio distance curves are therefore omitted in Fig. 10 and in the following. From Fig. 10 it can be clearly seen especially that the small observed amplitude ratios for the explosions from the Nevada Test Site and the upper limit values for observation distances around 79° cannot be explained by the model curves denoted with $Q_\alpha = 826$. Therefore, the question arises of changing which parameter or combination of parameters can the small amplitude ratios required by the data be obtained.

Amplitudes of PcP due to changes in the elastic parameters on both sides of the CMB

The question of the behaviour of the reflection amplitude to changes of the elastic parameters (P and S velocities and densities) on both sides of the CMB can be answered with sufficient accuracy by calculating partial derivatives of the plane-wave reflection coefficient R_{PP} of the CMB of model PREM. A small relative change of R_{PP} is a linear combination of small relative changes of the velocities and densities on both sides of the CMB (Müller et al., 1977)

$$\frac{\Delta R_{PP}}{R_{PP}} = c_1 \frac{\Delta \alpha_m}{\alpha_m} + c_2 \frac{\Delta \rho_m}{\rho_m} + c_3 \frac{\Delta \beta_m}{\beta_m} + c_4 \frac{\Delta \alpha_c}{\alpha_c} + c_5 \frac{\Delta \rho_c}{\rho_c} + c_6 \frac{\Delta \beta_c}{\alpha_c}, \quad (5)$$

where subscript m refers to parameters above, and subscript c to parameters below the CMB. Changes in β_c are normalized by α_c (Eq. 5) because $\beta_c = 0$ for model PREM. The coefficients $c_1, \ldots c_6$ are given in Table 3 for three different angles of incidence at the CMB and, hence, epicentral distances of PcP. The coefficients are a measure of the influence of the corresponding parameter on the amount of R_{PP}, and some important properties of the CMB reflecion coefficient can be derived from Table 3. The greatest change in the reflection amplitude (in the sense of a reduction) is caused by positive changes (i.e. by an increase) of the P-waves velocity α_m in the mantle and the S-wave velocity β_c in the core. Changes in the densities on both sides of the CMB and of the P-wave velocity α_c in the core have minor influence and can be neglected in our discussion. The reduction of the reflection amplitude caused by an increase of the velocity α_m is nearly compensated by an increase of the S velocity β_m. This means that the reflection amplitude cannot be reduced arbitrarily by increased P-velocity gradients in the lowermost mantle, when the S-velocity gradients are increased at the same time to obtain still reasonable Poisson's ratios. The dashed velocity-depth model of Fig. 8 is an attempt to explain the small observed PcP/P amplitude ratios by increased positive velocity gradients. The resulting theoretical PcP/P amplitude-ratio curve is presented in Fig. 10 for the distance range 70°–75°. Obviously, the small amplitude ratios required by the data cannot be explained through increased velocity gradients in a physically reasonable frame. The greatest reduction of the reflection amplitude (Table 3) can be achieved through the introduction of a non-zero S-wave velocity in

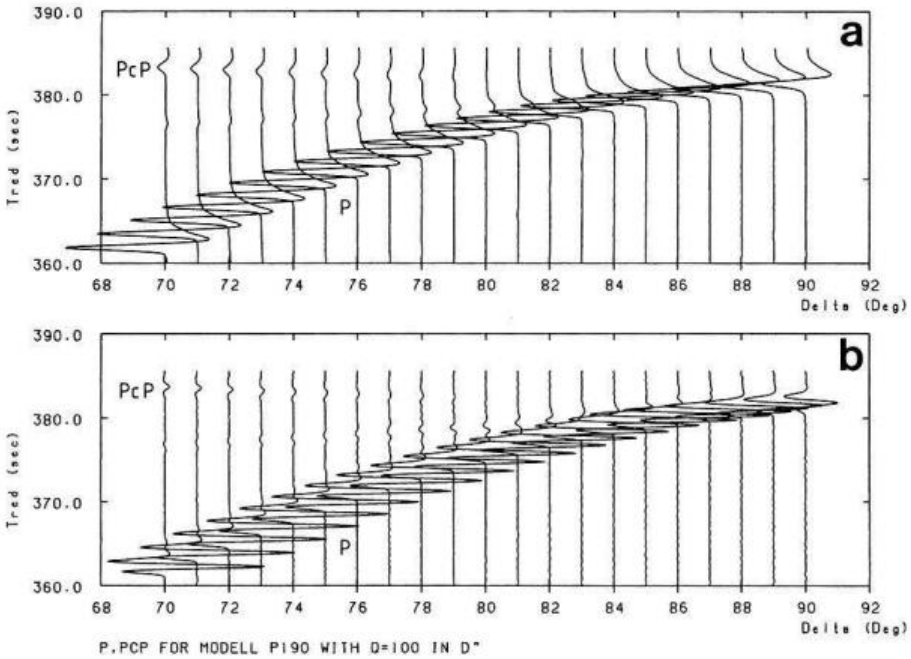

Fig. 9. a Theoretical record section (vertical component of particle velocity) for model P190 with $Q_\alpha = 100$ in D''. The focal mechanism is of thrust type with the *T*-axis vertical and the profile is perpendicular to the strike of the *P* nodal planes. The dominant period of the source pulse (i.e. the rise time of the moment function) is 1 s. **b** Simulation of the seismograms from **a** according to the transfer function of a short-period WWSSN seismometer

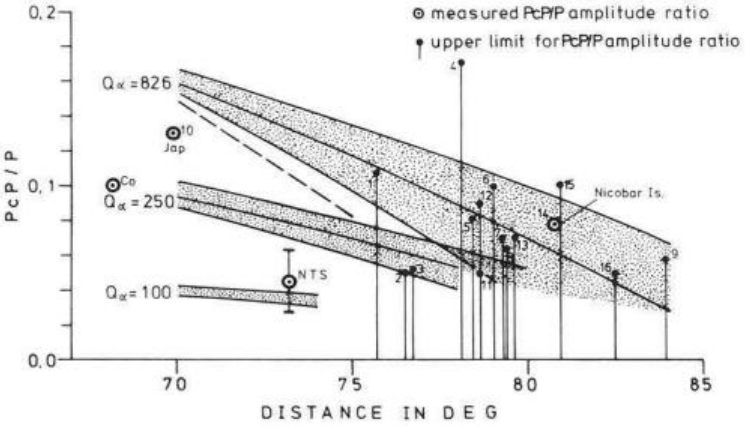

Fig. 10. The same as Fig. 7 with theoretical *PcP/P* amplitude-ratio distance curves superimposed. The *uppermost stippled band* (denoted $Q_\alpha = 826$) with three amplitude-ratio distance curves has been calculated (from above to below) for models N190, M190, P190 with the Q_α value of 826 in a D'' zone of 190 km thickness. The *dashed curve* corresponds to the model with the extreme, positive velocity gradient in Fig. 8. The two stippled bands denoted $Q_\alpha = 250$ and $Q_\alpha = 100$ are again calculated for the models (from above to below) N190, M190 (missing in the lowermost stippled band) and P190, but with Q_α values in D'' as indicated on the left. All theoretical curves correspond to isotropic radiation

Table 3. The plane-wave reflection coefficient R_{PP} of the CMB of model PREM and the coefficients $c_1, \ldots c_6$ in Eq. (5)

	R_{PP}	$c_1(\alpha_m)$	$c_2(\rho_m)$	$c_3(\beta_m)$	$c_4(\alpha_c)$	$c_5(\rho_c)$	$c_6(\beta_c)$
$\varphi = 72.5°$ $\Delta = 70°$	0.369	− 6.98	−1.02	5.69	1.15	0.81	− 8.31
$\varphi = 75.5°$ $\Delta = 75°$	0.321	− 8.41	−0.94	7.40	1.56	1.13	−10.60
$\varphi = 78.5°$ $\Delta = 80°$	0.247	−12.15	−1.52	10.22	2.02	1.26	−15.82

φ, angle of incidence at the core-mantle boundary; Δ, epicentral distance of *PcP* (focal depth 80 km)

the core. This more theoretical possibility for reducing the *PcP/P* amplitude ratio will not be considered further because it is in contrast to the results of independent seismological investigations by Müller et al. (1977) and Doornbos and Mondt (1979a). From this numerical investigation of the reflection coefficient of the CMB it can be concluded that physically meaningful variations of the elastic parameters on both sides of the CMB fail to reduce the theoretical *PcP/P* amplitude ratios to the level of the majority of the observed amplitude ratios.

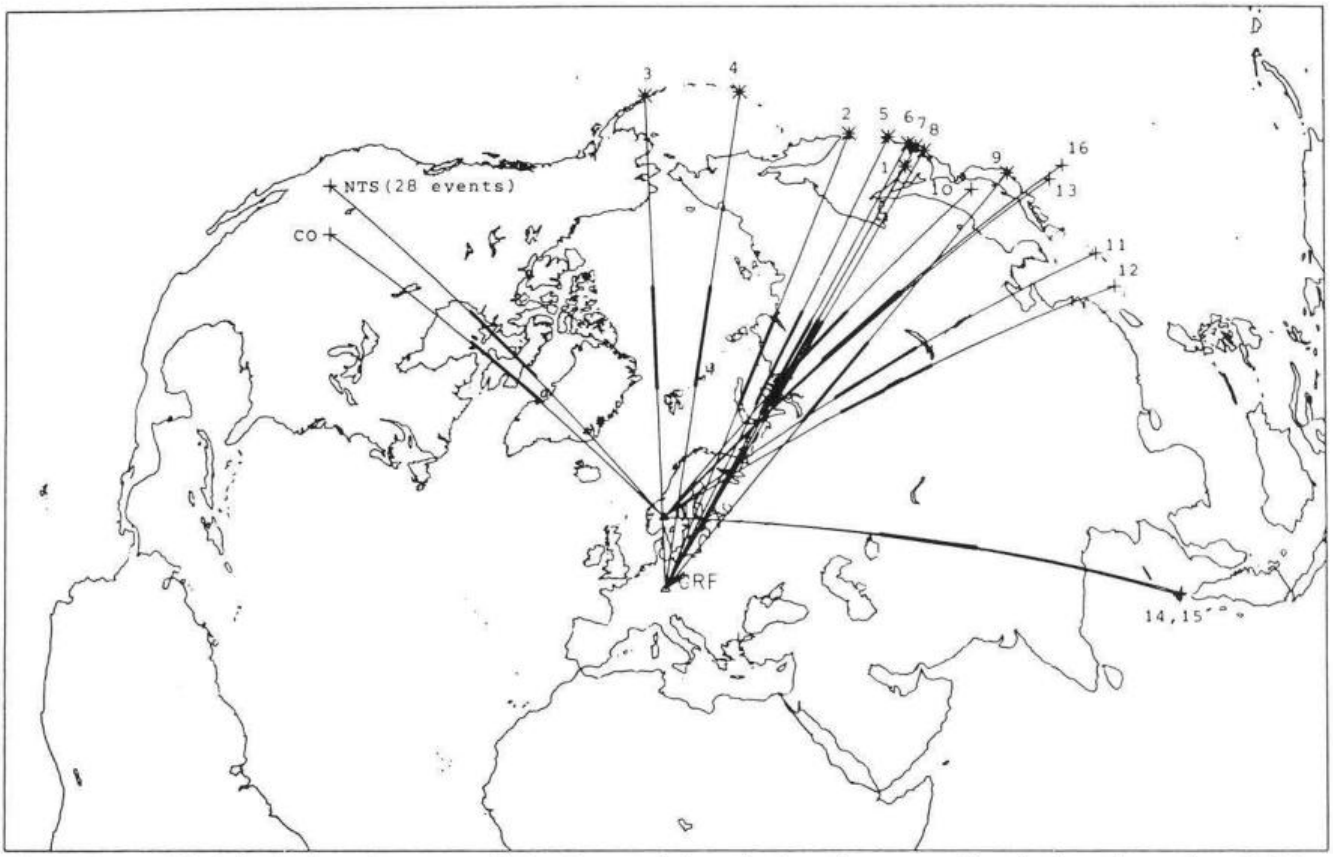

Fig. 11. Geographical distribution of events studied and great circle paths from the sources (* and +) to the receivers (GRF and NOA). Numbering of earthquake epicentres (Nos. 1–16) is according to Table 1. 'NTS' and 'Co' correspond to the epicentres of the nuclear explosions at the Nevada Test Site and Colorado, respectively. The lateral extent of that part of the ray path that *PcP* spends in a 190-km-thick D'' zone has been calculated and is marked with a *thick line*. The projection used is azimuthal equidistant with GRF as a projection pole

Increased absorption in D''

Another means to reduce the PcP/P amplitude ratio is the introduction of zones of reduced Q below the turning point of the mantle P wave. This leads to a relative increase of the dissipation time t^*_{PcP} of PcP compared to the dissipation time t^*_P of P. The resulting stronger damping of the reflection amplitude then gives the reduced PcP/P amlitude ratio. To evaluate this effect quantitatively we have calculated theoretical record sections for the models N190, M190 and P190 with Q_α values of 250 and 100 in a 190-km-thick D'' zone at the base of the mantle. The result is shown in Fig. 9a for the model P190 with $Q_\alpha = 100$. The dominant period of the source-time function for this and all other calculations was 1 s. Because of the low-pass effect of anelastic damping, the original 1-s dominant period of the double-couple source is broadened to an 'observed' dominant period of approximately 5 s in the particle-velocity seismogram (Fig. 9a). However, to enable a realistic comparison of observed and theoretical amplitude ratios it is important that the dominant periods in observed and theoretical seismograms are identical. This is especially important in our cases where the dissipation times of P and PcP are different and one obtains, therefore, different PcP/P amplitude ratios for different dominant periods. Figure 9b shows short-period simulations of the original seismograms from Fig. 9a according to the transfer characteristic of a WWSSN-SP system. To guarantee the condition of equal frequency content in observed and theoretical seismograms, the theoretical amplitude ratios (Fig. 10) were determined by measuring peak-to-peak amplitudes from such filtered synthetic seismograms. As can be seen from the narrow width of the stippled band of curves for $Q_\alpha = 100$ in Fig. 10, a discrimination between different velocity gradients becomes impossible under the regime of such low Q_α values. Moreover, it can be concluded from Fig. 10 that observed PcP/P amplitude ratios which are smaller than those predicted for nearly elastic models (e.g. those for $Q_\alpha = 826$) cannot be interpreted uniquely with respect to the velocity structure, because the amplitude-ratio distance curve for the elastic models can be shifted to lower or higher values through combination with lower or higher Q_α values within D''. On the other hand, the estimation of Q from the observed small amplitude ratios is possible with some reliability if one accepts models P190 and N190 as limiting the globally valid range for gradient models, as suggested by several investigations (Doornbos and Mondt, 1979; Mula and Müller, 1980; Mula, 1981; Doornbos, 1983).

Interpretation

The main result of the comparison of observed and theoretical PcP/P amplitude ratios in Fig. 10 is that a unique interpretation of the complete data set with one radially symmet-

ric model cannot be given. In Fig. 11 the ray-paths of all events used in this study are marked on a map of the northern hemisphere. The lateral extent of the ray path that *PcP* passes through D″ has been calculated (approximately 1,500 km at the surface) and is marked with a thick line in Fig. 11. We begin the interpretation of the data in Fig. 10 with those four data points for which *PcP* could reliably be identified. Among them are the amplitude ratios for the NTS and Colorado nuclear explosions, which are in close azimuthal neighbourhood. The mean *PcP*/*P* amplitude ratio for the observation geometry NTS-NORSAR is explained by Q_α values around 100 in D″. According to Fig. 11 this value and the Q_α value of 250 for the Colorado explosion is representative for the region on the CMB below the northern Hudson Bay. The earthquake in the Sea of Japan (No. 10) lies within the bulk of events with reflection points on the CMB below Central Siberia. The Nicobar Island earthquake (No. 14) has its *PcP* reflection point on the CMB below Usbekistan. It is the only event whose amplitude ratio falls within the range of theoretical amplitude ratios for models with a nearly elastic structure at the base of the mantle (Fig. 10). It is best explained by models M190 or N190 with a *Q* structure in D″ similar to that of PREM. The relatively small *PcP*/*P* amplitude ratio for the Sea of Japan earthquake (No. 10) cannot be explained with a nearly elastic structure at the base of the mantle. Q_α values of approximately 450 would lower the medium curve (model M190) of the uppermost stippled band in Fig. 10 to the observed amplitude ratio.

The events without identifiable *PcP* signal have their reflection points mainly below Central Siberia, except for events 3 and 4 which have their reflection points below the Arctic (Fig. 11). Despite the detailed investigation of the *PcP* beams and correlograms, practically no evidence for the existence of a *PcP* signal for these events could be found in the predicted arrival-time window. The corresponding data points in Fig. 10 are therefore interpreted as an upper limit for the true *PcP*/*P* amplitude ratio. On this background, the upper-limit estimates for the events with reflection points mainly below Central Siberia are interpreted by reduced Q_α values around 100, similar to the values found for the region below the northern Hudson Bay. For the region below the Arctic, only one upper limit value (no. 3 in Figs. 10 and 11) can be evaluated. The value for earthquake No. 4 cannot be interpreted because the *P*-wave-coda noise level in the arrival-time window for *PcP* is still high for this event (Fig. 5), so that the PHIMAX value exceeds the *PcP*/*P* amplitude ratio for all discussed models. A reliable interpretation for the region below the Arctic is impossible. However, Q_α values in D″ around 800 as in PREM, in connection with gradient models P190, M190 or N190, are unlikely.

It should be mentioned here that another mechanism besides anelastic absorption may be important for the low observed *PcP*/*P* amplitude ratios. Scattering of wide-angle *PcP* by the core-mantle boundary might distort the waveform of *PcP* so that matched filtering is no longer adequate. So far no quantitative calculations for this problem are known and one can argue against this only by observational evidence. The observations of *P* and *PcP* by several authors (e.g. Kanamori, 1967; Chowdhury and Frasier, 1973; Engdahl and Johnson, 1974) in general show an exact reproduction of *P* and *PcP* signal wave-forms, but these data examples stem mainly from the steep-angle range. However, the seismogram examples presented by Frasier and Chowdhury (Fig. 3, 1974) are an exception with respect to distance: they demonstrate impressively that the duplicity of *P* and *PcP* wave-forms holds up to distances of more than 70°. For the cases where *PcP* could be identified (Fig. 2) in this paper, the wave-forms of *P* and *PcP* are also very similar. This demonstrates that undulations on, or inhomogeneities near, the core-mantle boundary (if they exist for the sampled regions) have little influence on the wave-form of *PcP* even in the wide-angle range.

Evidence against discontinuities in the lowermost mantle from observations of short-period *P*

Several recent seismological investigations of the *P*- and *S*-wave velocity of the lowermost 200–300 km of the mantle have suggested velocity models with first-order discontinuities some hundred kilometres above the core- mantle boundary. The per cent velocity increase at such first-order discontinuities ranges from approximately 1.5% (Wright and Lyons, 1981) to 2.5%–3.0% (Wright et al., 1985) for the *P*-wave velocity (170 km above the core) and from 2.5%–3.0% (Lay and Helmberger, 1983a, b) for the *S*-wave velocity (280 km above the core). The *P*-velocity results, which hold for *P* waves recorded at the Yellowknife array (bottoming beneath the Carribean) and for *P* waves recorded at a temporary network in Australia (bottoming beneath southeast Asia), were derived using special array data-processing methods (Wright and Lyons, 1981; Wright et al., 1985). The *S*-velocity results, which hold for three separate regions of D″ (beneath Alaska, northern Eurasia and the Carribean) were derived by modelling the amplitudes and travel times of onsets between mantle *S* and *ScS* in transverse-component seismograms at distances from 70° to 80° (Lay and Helmberger, 1983a).

High-quality short-period *P*-wave data offer another means to study the reality of discontinuities in the lowermost mantle. Lay and Young (1986) argue that the *S*-wave velocity discontinuity in SLHO may be accompanied by a relatively smaller *P*-velocity increase. This possibility, which holds only to the extent that the change in bulk modulus is significantly less than the change in rigidity [cf. formula (1) in Schlittenhardt et al., (1985)], can be tested with the array data compiled for this study. No special array data-processing methods are needed, simple beamforming is sufficient to demonstrate the effects.

The model SLHO of Lay and Helmberger (1983a) is shown in Fig. 12 together with the corresponding *P* travel-time curve for an earthquake at 80 km depth. The jumps in *S* and *P* velocity at the discontinuity are both 2.6%. For this model and a model with a reduced *P*-velocity jump of 1.3% (keeping all other parameters unchanged), we have computed short-period theoretical seismogram sections for *P* waves (Fig. 13). As expected from the travel-time curve in Fig. 12, the record sections in Fig. 13 show pronounced differences between SLHO and models with smooth velocity-depth functions in the lowermost mantle. Near the shadow boundary (at $\Delta \approx 95°$), SLHO predicts three onsets with approximately equal magnitudes, whose arrival-time differences are great enough to be resolvable with a standard short-period instrument. The first of the three onsets (Figs. 12 and 13) is the diffraction P_{diff} along the CMB. It is followed by the phase labelled *PDDP*, which is reflected once at the underside of the discontinuity. This phase is

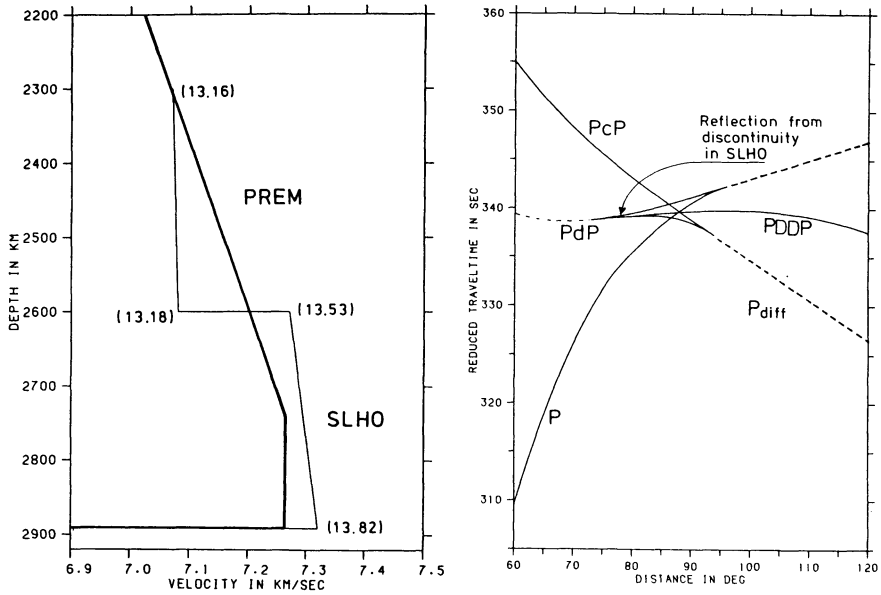

Fig. 12. *Left:* *S*-wave velocity distribution in the lowermost mantle for the models SLHO of Lay and Helmberger (1983a) and PREM (Dziewonski and Anderson, 1981). Velocity values in parentheses are assumed SLHO*P*-wave velocities. The jumps in *S* and *P* velocity at the discontinuity of SLHO are both 2.6%. Elsewhere in the earth, SLHO and PREM agree. *Right*: *P*-wave travel times for SLHO and a focal depth of 80 km (reduced with 4.8 s/deg). For explanation of the phases, see text

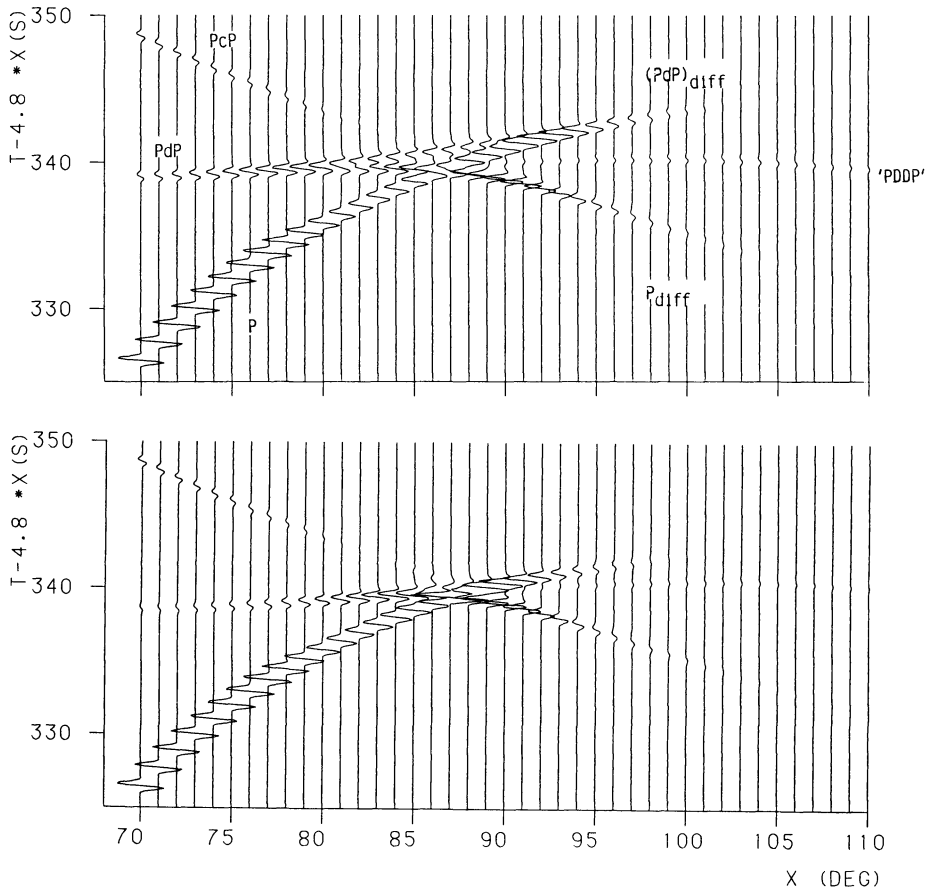

Fig. 13. Theoretical record sections for the SLHO model from Fig. 12 with jumps in *S* and *P* velocity both of 2.6% (*above*) and a reduced *P*-velocity jump of 1.3% (*below*), with all other parameters kept unchanged. The theoretical seismograms were computed with the reflectivity method and correspond to a focal depth of 80 km, the focal mechanism is of normal-fault type with the *P*-axis vertical and the profile is perpendicular to the strike of the *P* nodal planes. Times are reduced with 4.8 s/deg. The phases *PdP*, $(PdP)_{diff}$ and *PDDP* are caused by the discontinuity in SLHO (see text)

analogous to the phases *PKKP* or *SKKS* which are reflected once at the underside of the CMB. Note that at distances beyond $\Delta \approx 100°$ the amplitudes of *PDDP* are greater than those of P_{diff} in both sections of Fig. 13. The third onset is the diffraction $(PdP)_{diff}$ along the discontinuity (the letters *d* and *D* represent the depth of the discontinuity in SLHO). From Figs. 12 and 13 it is obvious that a test of SLHO with short-period *P*-wave data can be performed for the distance range near the core shadow zone. It appears that even the model with the 1.3% velocity increase at the discontinuity, in such an investigation, will prove to be inconsistent with short-period *P*-wave data available for arrays. In the following we will concentrate, however, on the distance range 70°–85°. The amplitude of the reflection from the discontinuity in SLHO (*PdP* in Figs. 12 and 13) increases from about 15% to over 90% of the amplitude of *P* in that distance range.

Events which are appropriate for a test of model SLHO

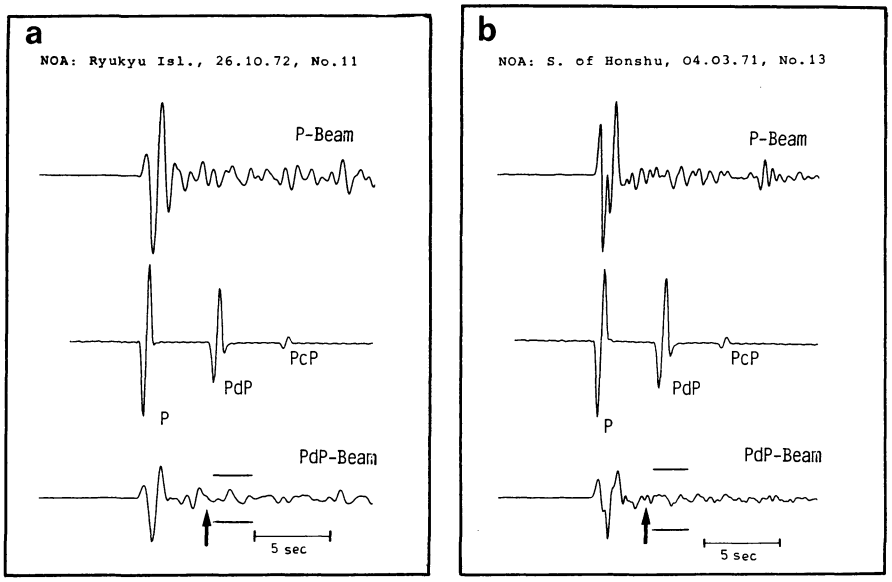

Fig. 14. a *P* beam (*uppermost trace*) and *PdP* beam (*lowermost trace*) for the Ryukyu earthquake (No. 11) at $\Delta = 78.6°$ and theoretical seismogram (*middle trace*) for the SLHO model of Lay and Helmberger (1983a) with jumps in *S* and *P* velocity both of 2.6%. *P* and *PdP* beam are plotted with equal amplitude scale. The peak-to-peak amplitude of the *P* signal in the theoretical seismogram in the middle is chosen to be identical with the maximum peak-to-peak amplitude of the *P* signal in the *P* beam. Hence, the amplitude of the theoretical *PdP* signal can be directly compared to the amplitudes in the *PdP* beam at the corresponding time interval. The pair of *horizontal bars* in the *PdP* beam indicates the peak-to-peak amplitude of *PdP*, predicted by a SLHO model with a reduced *P*-velocity increase of 1.3%. The phase *PdP*, predicted by model SLHO, is not observed, independently of whether the *S*-velocity jump of 2.6% is accompanied by a *P*-velocity jump of equal or half the size of that in the *S* velocity. **b** The same as in Fig. 14a for the earthquake south of Honshu at $\Delta = 79.6°$

must have, as in the investigation of *PcP*, a short source pulse compared to the difference travel time *PdP-P*. Simple and, compared to the *PdP-P* time, short *P* pulses are found for the NORSAR events 11 and 13. As the slownesses of *PdP* and *P* are different, *P*-coda amplitudes at the arrival time of *PdP* can be suppressed by *PdP* beam-forming. Although practically all events of this study, for distances from approximately 79° to 85°, can be used to disprove models with *P*-velocity jumps of 2.6% (e.g. compare the seismograms for events 7 and 14 in Figs. 2b and 5), in the following we will concentrate on the two events mentioned. From the travel-time curve in Fig. 12 we have derived the slowness-versus-distance curve for model SLHO (Schlittenhardt, 1984) to compute the NORSAR array beam fot the phase *PdP* for events 11 and 13. Figure 14a and b shows a comparison of the *P*, *PdP* beam and the theoretical seismograms for model SLHO with a velocity increase of 2.6% for both the *S* and *P* velocity for the observation distances of 78.6° and 79.6°. The *P* and *PdP* beams are plotted with the same amplitude scale. The *P* amplitude in the *PdP* beams is reduced to approximately 50% of its value. The pair of horizontal bars in the *PdP* beams of Fig. 14 indicates the peak-to-peak amplitude of *PdP* prdicted by the SLHO model with a reduced *P* velocity increase of 1.3%. Figure 14 demonstraties clearly that the complications expected for SLHO-type models are not observed for *P* waves bottoming beneath Central Siberia, irrespective of the *S*-velocity jump being accompanied by a *P*-velocity jump of equal or half the size of that in the *S* velocity.

Summary and conclusions

In this study the amplitude ratio *PcP*/*P* in the distance range 70°–84° has been investigated for several regions on the core-mantle boundary. For stations in this distance range, *PcP* spends about 900 km in a 190-km-thick D″ zone. A main result of this investigation is that one radially symmetric model cannot simultaneously explain observations from different geographical regions. Hence, lateral heterogeneity must exist in the lowermost mantle. It turnes out that this lateral heterogeneity in D″ cannot only be restricted to the velocity structure [as was found e.g. by Dziewonski (1984) by inversion of a great amount of catalogued *P*-wave travel times], but that significant lateral variations in wave absorption within D″ must exist. This follows from the fact that most of the observed, very small *PcP*/*P* amplitude ratios cannot be explained by physically reasonable variations of the elastic parameters on both sides of the CMB. The results, in detail, are as follows. Values of Q_α of about 100 were found for D″ for the region below the northern Hudson Bay (NTS-NORSAR profile) with lateral variations to Q_α values around 250 (Colorado-NORSAR profile). Comparable low Q_α values around 100 were found for a more wide-spread region below Central Siberia (Sea of Okhotsk-GRF, Kuriles-GRF and Japan-NORSAR profiles) with lateral variations to $Q_\alpha \approx 450$ (Sea of Japan-NORSAR profile). The only region with normal wave absorption (in the sense of the PREM model which has Q_α around 800 in D″) is the region below Usbekistan, USSR (Nicobar Island-NORSAR profile). Only for this region, with nearly elastic conditions at the base of the mantle, is a statement about the *Q and* velocity structure possible. Compared to the velocity gradients in the main part of the lower mantle, slightly reduced velocity gradients were found for this region, whose values are limited by the values for the models M190 and N190 (Fig. 8).

The comparison of short-period synthetic seismograms for models with first-order discontinuities near the top of

D″ (e.g. as suggested by Wright and Lyons, 1981; Lay and Helmberger, 1983a, b; Wright et al. 1985; Lay and Young, 1986) with the short-period array data compiled for this study leads to a clear refutation of such models if the *P*-velocity jump at the discontinuity is of the order of 2.5%–3.0%, as was already concluded from a study of long-period diffracted *P* waves (Schlittenhardt et al., 1985). Such models are very unlikely to be a global feature. Even if the *P*-velocity jump is halved, to 1.3%, data examples which do not show the predicted effects can be found. These seismogram examples correspond to ray paths bottoming beneath Central Siberia.

Acknowledgements. I am grateful to Gerhard Müller for suggesting this study and for his support in the course of this work. I thank Peter Hubral for reading the manuscript and Rainer Kind for valuable comments. The staff of the NTNF/NORSAR Data Processing Center and the Seismologisches Zentralobservatorium Gräfenberg offered helpful support. This research was supported by a grant from the Deutsche Forschungsgemeinschaft. All this is gratefully acknowledged.

References

Aki, K., Richards, P.G.: Quantitative seismology, theory and methods. Vol. I and II, Freeman and Co., 1980

Alexander, S.S., Phinney, R.A.: A study of the core-mantle boundary using P waves diffracted by the earth's core. J. Geophys. Res. **71**, 5943–5958, 1966

Berzon, I.S., Kogan, S.P., Pasechnik, I.P.: The character of the mantle-core boundary from observations of PcP waves. Earth Planet. Sci. Lett. **16**, 166–170, 1972

Bolt, B.A.: PdP and PKiKP waves and diffracted PcP waves. Geophys. J. R. Astron. Soc. **20**, 367–382, 1970

Buchbinder, G.G.R.: Properties of the core-mantle boundary and observations of PcP. J. Geophys. Res. **73**, 5901–5923, 1968

Buchbinder, G.G.R., Poupinet, G.: Problems related to PcP and the core-mantle boundary illustrated by the two nuclear events. Bull. Seismol. Soc. Am. **63**, 2047–2070, 1973

Bullen, K.E.: Compressibility-pressure hypothesis and the earth's interior. Month. Not. R. Astron. Soc. Geophys. Suppl. **5**, 355–368, 1949

Bullen, K.E.: An earth model based on a compressibility-pressure hypothesis. Month. Not. R. Astr. Soc. Geophys. Suppl. **6**, 50–59, 1950

Chowdhury, D.K., Frasier, C.W.: Observations of PcP and P at Lasa at distances from 26° to 40°. J. Geophys. Res. **78**, 6021–6027, 1973

Cleary, J.R.: The S velocity at the core-mantle boundary from observations of diffracted S. Bull. Seismol. Soc. Am. **59**, 1399–1405, 1969

Cormier, V.F.: Some problems with S, SKS and ScS observations and implications for the structure at the base of the mantle and the outer core. J. Geophys. **57**, 14–22, 1985

Doornbos, D.J.: On seismic wave scattering by a rough core-mantle boundary. Geophys. J. R. Astron. Soc. **53**, 643–662, 1978

Doornbos, D.J.: Present seismic evidence for a boundary layer at the base of the mantle. J. Geophys. Res. **88**, 3498–3505, 1983

Doornbos, D.J., Husebye, E.S.: Array analysis of PKP phases and their precursors. Phys. Earth Planet. Inter. **5**, 387–399, 1972

Doornbos, D.J., Mondt, J.C.: Attenuation of P and S waves diffracted around the core. Geophys. J. R. Astron. Soc. **57**, 353–379, 1979a

Doornbos, D.J., Mondt, J.C.: P and S waves diffracted around the core and the velocity structure at the base of the mantle. Geophys. J. R. Astron. Soc. **57**, 381–395, 1979b

Dziewonski, A.M.: Mapping the lower mantle: determination of lateral heterogeneity in P velocity up to degree and order 6. J. Geophys. Res. **89**, 5929–5952, 1984

Dziewonski, A.M., Anderson, D.L.: Preliminary reference earth model. Phys. Earth Planet. Inter. **25**, 297–356, 1981

Elsasser, W.M., Olson, P., Marsh, B.D.: The depth of mantle convection. J. Geophys. Res. **84**, 147–155, 1979

Engdahl, E.R., Johnson, L.E.: Differential PcP travel times and the radius of the core. Geophys. J. R. Astron. Soc. **39**, 435–456, 1974

Frasier, C.W., Chowdhury, D.: Effect of scattering on PcP/P amplitude ratios at Lasa from 40° to 84° distance. J. Geophys. Res. **79**, 5469–5477, 1974

Gutenberg, B., Richter, C.F.: On seismic waves. Gerlands Beitr. Geophys. **43**, 56–133, 1936

Haddon, R.A.W.: Evidence for inhomogeneities near the core-mantle boundary. Phil. Trans. Roy. Soc. Lond. **A306**, 61–70, 1982

Haddon, R.A.W., Cleary, J.R.: Evidence for scattering of seismic PKP waves near the mantle-core boundary. Phys. Earth Planet. Inter **8**, 211–234, 1974

Hales, A.L., Roberts, J.L.: The travel times of S and SKS. Bull. Seismol. Soc. Am. **60**, 461–489, 1970

Harjes, H.-P., Henger, M.: Array seimology. J. Geophys. **39**, 865–905, 1973

Ibrahim, A.K.: The amplitude ratio PcP/P and the core-mantle boundary. Pageoph. **91**, 114–133, 1971

Ibrahim, A.K.: Evidence for a low velocity core-mantle transition. Phys. Earth Planet. Inter. **7**, 187–198, 1973

Jeanloz, R., Richter, F.M.: Convection, composition and the thermal state of the lower mantle. J. Geophys. Res. **84**, 5497–5504, 1979

Jones, G.M.: Thermal interaction of the core and the mantle and long-term behaviour of the geomagnetic field. J. Geophys. Res. **82**, 1703–1709, 1977

Kanamori, H.: Spectrum of P and PcP in relation to the mantle-core boundary and attenuation in the mantle. J. Geophys. Res. **72**, 559–571, 1967

Kanasewich, E.R.: Time sequence analysis in geophysics. University of Alberta Press, 1975

Kelly, E.J.: Response of seismic arrays to wide-band signals. Linc. Lab. Techn. Note 30, 1967

King, D.W., Haddon, R.A.W., Cleary, J.R.: Array analysis of precursors to PKIKP in the distance range 128° to 142°. Geophys. J. R. Astron. Soc. **37**, 157–173, 1974

Lay, T., Helmberger, D.V.: A lower mantle S-wave triplication and the shear velocity structure of D″. Geophys. J. R. Astron. Soc. **75**, 799–837, 1983a

Lay, T., Helmberger, D.V.: The shear velocity gradient at the base of the mantle. J. Geophys. Res. **88**, 8160–8170, 1983b

Lay, T., Young, C.J.: The effect of SKS scattering on models of the shear velocity structure of the D″ region. J. Geophys. **59**, 11–15, 1986

Lüke, H.D.: Signalübertragung, Heidelberg: Springer-Verlag 1979

Mitchell, B.J., Helmberger, D.V.: Shear velocities at the base of the mantle from observations of S and ScS. J. Geophys. Res. **78**, 6009–6027, 1973

Mondt, J.L.: SH-waves: theory and observations for epicentral distances greater than 90 degrees. Phys. Earth Planet. Inter. **15**, 46–59, 1977

Müller, G., Mula, A.H., Gregersen, S.: Amplitudes of long-period PcP and the core-mantle boundary. Phys. Earth Planet. Inter. **14**, 30–40, 1977

Müller, G.: The reflectivity method: a tutorial. J. Geophys. **58**, 153–174, 1985

Mula, A.H.: Amplitudes of diffracted long-period P and S waves and the velocities and Q-structure at the base of the mantle. J. Geophys. Res. **86**, 4999–5011, 1981

Mula, A.H., Müller, G.: Ray parameters of diffracted long-period P and S waves and the velocities at the base of the mantle. Pageoph. **118**, 1270–1290, 1980

Okal, E.A., Geller, R.J.: Shear wave velocity at the base of the mantle from profiles of diffracted SH-waves. Bull. Seismol. Soc. Am. **69**, 1039–1053, 1979

Peltier, W.R., Jarvis, G.T.: Whole mantle convection and the thermal evolution of the earth. Phys. Earth Planet Inter. **29**, 281–304, 1982

Phinney, R.A., Alexander, S.S.: P wave diffraction theory and the structure of the core-mantle boundary. J. Geophys. Res. **71**, 5959–5975, 1966

Sacks, I.S.: Diffracted P wave studies of the earth's core, 2. lower mantle velocity, core size, lower mantle structure. J. Geophys. Res. **72**, 2589–2594, 1967

Schlittenhardt, J.: Array-Untersuchungen von reflektierten und diffraktierten Kernphasen. PhD thesis. University of Frankfurt, 1984

Schlittenhardt, J., Schweitzer, J., Müller, G.: Evidence against a discontinuity at the top of D″. Geophys. J. R. Astron. Soc. **81**, 295–306, 1985

Seidl, D.: The simulation problem for broad-band seismograms. J. Geophys. **48**, 84–93, 1980

Spies, T.: Untersuchung der seismischen Geschwindigkeiten an der Basis des Mantels mit Amplituden und Laufzeiten der Kernreflexion PcP. Diploma Thesis. University of Frankfurt, 1985

Wright, C., Lyons, J.A.: Further evidence for radial velocity anomalies in the lower mantle. Pageoph. **119**, 137–162, 1981

Wright, C., Muirhead, K.J., Dixon, A.E.: The P wave velocity structure near the base of the mantle. J. Geophys. Res. **90**, 623–634, 1985

Received January 24, 1986; revised version May 20, 1986
Accepted May 23, 1986